GDC-Based Infiltrated Electrodes for Solid Oxide Electrolyzer Cells (SOECs)

Luca Spiridigliozzi [1,*] **, Elisabetta Di Bartolomeo** [2,3] **, Gianfranco Dell'Agli** [1,3]
and Francesca Zurlo [2]

[1] Department of Civil and Mechanical Engineering, University of Cassino and Southern Lazio, Via G. Di Biasio 43, 03043 Cassino (FR), Italy; dellagli@unicas.it
[2] Department of Chemical Sciences and Technology, University of Roma Tor Vergata, 00133 Roma, Italy; dibartolomeo@uniroma2.it (E.D.B.); francesca.zurlo@uniroma2.it (F.Z.)
[3] National Interuniversity Consortium of Materials Science and Technology (INSTM), Via G. Giusti 9, 50121 Florence, Italy
* Correspondence: l.spiridigliozzi@unicas.it; Tel.: +39-39-3017-9150; Fax: +39-077-628-2880

check for updates

Abstract: In this work, porous complex and metal-free cathodes based on a $(La_{0.6}Sr_{0.4})(Cr_{0.5}Mn_{0.5})O_3$ (LSCM) screen-printed backbone infiltrated with $Ce_{0.9}Gd_{0.1}O_2$ (GDC) were fabricated for solid oxide electrolyzer cells. GDC infiltration has been optimized by structural and microstructural investigation and tested by electrochemical measurements in CO/CO_2 mixtures. Infiltrated electrodes with a non-aqueous GDC solution showed the best electro-catalytic activity towards CO_2 reduction, exhibiting a much lower polarization resistance, i.e., $R_{pol} = 0.3$ $\Omega \cdot cm^2$ at 900 °C. The electrochemical performance of LSCM/GDCE in terms of R_{pol} is comparable to the best-performing Ni-YSZ cathode in the same operating conditions ($R_{pol} = 0.23$ $\Omega \cdot cm^2$).

Keywords: SOEC; infiltration; doped-ceria; cathodes

1. Introduction

The electrochemical conversion of CO_2 for fuels and chemical production is one of the most promising methods for greenhouse gas recycling and reutilization [1]. Unfortunately, it is known that low-temperature electrochemical processes exhibit several major issues related to slow reaction kinetic, the strict control of operating conditions, and catalyst poisoning [2–4]. Low-temperature electrochemical processes for CO_2 reduction involving molecular catalysts or non-aqueous solvent systems have also been proposed, but they show some major drawbacks such as high costs and low current densities [5–7]. Otherwise, high-temperature solid oxide electrolyzer cells (SOECs) show several positive features: firstly, SOECs are whole-ceramic devices and do not make use of liquid electrolytes, avoiding the problem of leakage and corrosion [8,9]. Then, the high operating temperature favors the kinetic at the electrodes and increases the overall efficiency of the cells [10]. Finally, SOECs can exploit all advantages of the development of solid oxide fuel cell (SOFC) materials [11–13] and technologies [14,15]. Therefore, extensive studies of SOECs and CO_2 electrolysis are largely available in the recent literature [1,16,17], as durable, stable, and efficient working electrodes for SOEC are greatly required.

Nickel/yttria stabilized zirconia (Ni-YSZ) has been widely investigated and proposed as the best cathode material for SOECs, mainly because of its very good ionic and electronic conductivity, high catalytic activity, low cost, and an expansion coefficient comparable to those of other cell components. Despite the high CO_2 conversion efficiency, however, Ni-based electrodes have shown some severe limitations due to the strict requirements of fuel compositions

(to avoid Ni oxidation) and the carbon coke formation [18]. To replace Ni-based electrodes, perovskite materials such as variously doped lanthanum chromites or lanthanum ferrites and their mixtures have been recently investigated. They show good stability in carbon-rich environments and promising electro-catalytic activity for CO_2 conversion [19,20]. For example, perovskite oxides such as $(La_{0.75}Sr_{0.25})_{0.95}Cr_{0.5}Mn_{0.5}O_{3-\delta}$ [21], $La_{0.35}Sr_{0.65}TiO_{3-\delta}$ [22], $La_{0.6}Sr_{0.4}VO_{3-\delta}$ [23], and $Sr_2Fe_{1.5}Mo_{0.5}O_{6-\delta}$ [24] can represent valid alternatives to Ni-YSZ cathodes. In particular, these perovskite oxides exhibit high mixed electronic and ionic conductivity, very good redox stability, and a very high resistance to both sulfur poisoning and coke formation. Unfortunately, such perovskite-based cathodes do not reach a CO_2 electrolysis performance comparable to Ni-YSZ cathodes, mainly because of their reduced electrocatalytic activity.

However, recently, a novel composite cathode based on lanthanum strontium chromium manganite (LSCM)/gadolinium-doped ceria (GDC) seems to be a good alternative to Ni-YSZ cathodes [25]. It was already reported that the infiltration of GDC nanoparticles into the LSCM backbone is crucial because it increases the triple-phase boundaries (TPBs) and favors the CO_2 chemical adsorption [26,27], enhancing the electrochemical CO_2 dissociation. Nevertheless, the agglomeration of doped-ceria nanoparticles occurring upon preparation and/or long-term runs can affect the stability of the cell. Moreover, the morphological properties of GDC-infiltrated powders may also depend on the starting solutions used for the infiltration into the LSCM backbone [28]. Generally speaking, oxide particles precipitated from aqueous solutions often show a tendency to agglomerate [29,30] and, in the case of ceria-based systems, the use of non-aqueous solutions can give some advantages in terms of the morphology of the infiltrated powders [31].

In this work, we investigated the influence of different infiltrating solutions upon the electrode microstructure. Thus, aqueous and ethanol GDC solutions were used for the infiltration of the LSCM backbone deposited on an 8 mol% Y_2O_3-doped ZrO_2 (8YSZ) electrolyte. The morphology of the electrodes and the electrochemical performance of the cells are investigated and discussed.

2. Materials and Methods

8 mol% Y_2O_3-doped ZrO_2 (8YSZ) powders purchased from Tosoh were used as an electrolyte. The powders were uniaxially pressed into pellets and sintered at 1500 °C for 3 h using a heating rate of 2 °C/min. The density of the sintered pellets, measured with a hydrostatic balance, was 5.86 g/cm^3 (about 97% of the theoretical value). Thick electrodes were screen-printed onto both sides of the pellets. Scandium-doped Zirconia (ScSZ, Pi-Kem Ltd.—Tamworth, UK), YSZ (Tosoh—Tokyo, Japan), and Lanthanum Strontium Manganite (LSM, Pi-Kem Ltd.—Tamworth, UK) were employed for anode preparation and Lanthanum Strontium Chromium Manganite (LSCM, Pi-Kem Ltd.—Tamworth, UK) for the cathode. Inks for deposition were prepared by ball milling each powder with a dispersant (Polyester/Polyamide Copolymer Dispersant, KD-1) and organic binders (Terpineol and Decoflux WB41) [32]. Glassy carbon and graphite were used as a pore former. A total of 30 wt% of pore former was necessary to get sufficient porosity for infiltration. Solutions (2 M) of 10% mol Gd-doped CeO_2 (GDC10) were prepared for the cathode impregnation. Proper amounts of $Ce(NO_3)_3 \cdot 6H_2O$ (Sigma-Aldrich—Steinheim, Germany) and $Gd(NO_3)_3 \cdot 6H_2O$ (Sigma Aldrich—Steinheim, Germany), i.e., 19,537 and 2256 g for cerium nitrate and gadolinium nitrate, respectively, were dissolved into 25 mL of either distilled water (GDCW solution) or into pure ethanol (GDCE solution). Thus, the two solutions used for infiltration are named: GDCW and GDCE.

For the cathode fabrication, a thin first layer of YSZ was screen-printed onto the YSZ electrolyte pellet to favor a good adhesion with the overlaying LSCM layer. The deposited layers were soaked at 800 °C for 1 h to remove any undesired carbon residues and then co-fired at 1300 °C for 2 h. For the anode fabrication, a ScSZ layer was firstly screen-printed and then an LSM layer was successively added. Each layer was soaked at 800 °C for 1 h and the bilayer was co-fired at 1100 °C for 2 h using a heating rate of 2 °C/min. The thickness of both bilayer electrodes was about 30–40 μm.

The LSCM/YSZ backbone was infiltrated using two GDC precursor solutions. The infiltration steps were carried out at room temperature and at atmospheric pressure. After each infiltration step, a thermal treatment at 500 °C for 45 min was performed to let the nitrates decompose. After each firing, the cell was weighted in order to get the final GDC loading equal to 50% of the YSZ/LSCM bilayer weight. A final calcination step of 1 h at 1100 °C was performed.

Structural and microstructural characterizations of infiltrated cathodes were performed. X-Ray Diffraction (XRD) analysis was carried out with a X-Pert Pro 500 diffractometer (Philips—Amsterdam, Nederlands) to evaluate the presence of the undesirable crystalline phases. Field emission-scanning electron microscopy (FE-SEM) using a Leo Supra 35 (Zeiss—Oberkochen, Germany) was used to investigate the grain size and distribution of the GDC particles infiltrated into the LSCM/YSZ cathode.

For electrochemical measurements, the cells were fastened onto an alumina tube using a gas-tight ceramic paste (curing treatment of 150 °C for 3 h). Au paste and wires were used as current collectors. Electrochemical impedance spectroscopy (EIS) measurements at open circuit voltage (OCV) were collected using a frequency response analyzer (FRA, Solartron 1260—Solartron Analytical—Leicester, UK) coupled with a dielectric interface (Solartron 1296—Solartron Analytical—Leicester, UK) with a frequency range of between 0.1 Hz and 1 MHz and an AC voltage amplitude of 100 mV. The measurements were carried out in the 700–800 °C temperature range, exposing the cathode to a 30/70 volume ratio of CO/CO_2 and the anode to static air.

3. Results and Discussion

GDC loading by infiltration varies considerably when using water and ethanol as solvents. Figure 1 shows the GDC loading percentage vs. the number of infiltrations by using the GDCW and GDCE solutions. The infiltrated cathodes are named LSCM/GDCW and LSCM/GDCE. The target value corresponding to the 50 wt% of the YSZ/LSCM weight is 100%. By using the GDCE solution, the desired amount of GDC loading was reached with five infiltrations, while eight infiltrations were necessary for the GDCW solution. For each infiltration step, the same liquid volume was selected. Moreover, the difference in the wetting behavior of the electrode support at each infiltration step is noteworthy. In fact, the GDCE droplets almost immediately diffused all over the support surface, while the liquid–solid interaction between the support and GDCW was significantly lower, as the liquid droplets had to be gently deposited in different electrode sites to obtain a homogeneous distribution of the infiltrated volume. The GDCE infiltration process produced a constant rate loading, while the GDCW infiltration showed a strongly non-linear loading evolution. The linear trend in the case of the GDCE suggests that the superficial region of the sample is substantially unaltered by the sequence of the infiltration steps, whereas the parabolic behavior likely indicates the formation of some barriers that reduce the further loading. Stoyanova et al. observed that factors such as the volatility of the impregnating medium (solution) may affect the distribution of the impregnated phase, i.e., ethanol ensured a small blocking effect of the porous texture and, thus, a high specific surface area of the impregnated phase [33].

The LSCM/GDCW- and LSCM/GDCE-infiltrated cathodes with the same GDC amount were investigated by XRD analysis. Figure 2 shows the XRD pattern of the LSCM/GDCW infiltrated cell. The LSCM/GDCE cell exhibits an identical diffraction pattern and thus, for reasons of clarity, it is not reported. All peaks belong to the 8YSZ (ICDD card n. 30-1468), GDC (ICDD card n. 75-161), and LSCM (ICDD card n. 86-1552) phases and no secondary phase has been revealed. Cerium and gadolinium mixed in the proper amount into the infiltrating solution formed a perfect homogeneous solid solution with a mild calcination step. The crystallographic parameter of cubic GDC was determined using UnitCell software [34]. The calculated value was 0.54177(1) nm in very good agreement with the theoretical value (0.5418 nm according to ICDD card n. 75-161), confirming the homogeneous dissolution of Gd^{3+} cations in the fluorite lattice of ceria. The crystallite size was calculated using the Scherrer equation for the most intense peak, i.e., (111) at $2\theta = 28.5°$. The size was about 80 nm for

both the LSCM/GDCW and LSCM/GDCE cathodes, meaning that no significant difference in the grain size was detectable for the two impregnation methods.
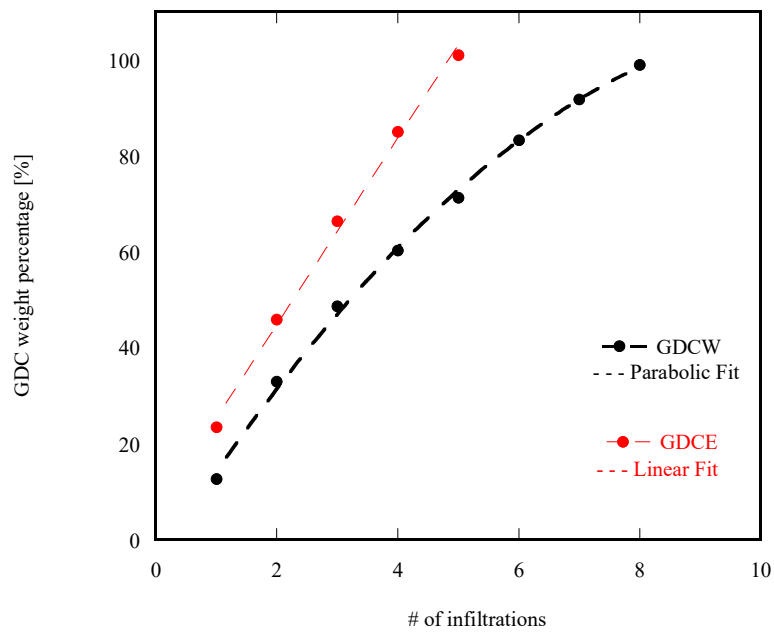

Figure 1. Weight gain of the lanthanum strontium chromium manganite/distilled water (LSCM/GDCW) and LSCM/pure ethanol (GDCE) electrodes as a function of the infiltration steps.
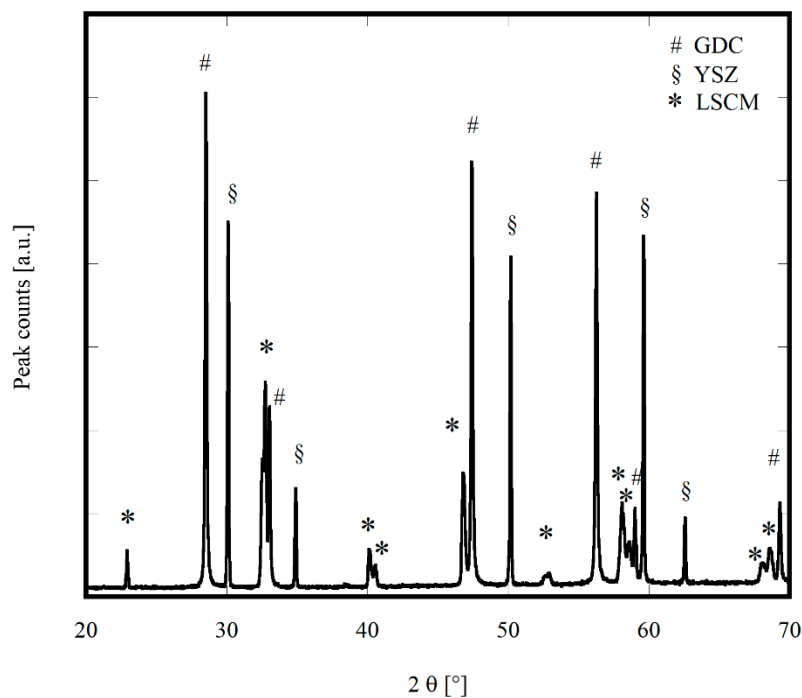

Figure 2. XRD pattern of the LSCM/GDCW infiltrated electrode.

Microstructural analyses of the cathode/electrolyte interface and cathode surface were performed. Figure 3 shows the SEM micrograph of a 30 μm thick LSCM/GDCW cross section. A very good adhesion between cathode and electrolyte is reasonably revealed due to the presence of a thin YSZ screen-printed layer. The same features (not reported) were also revealed for the LSCM/GDCE cathode, indicating that no significant difference appears from the cross-section analysis.
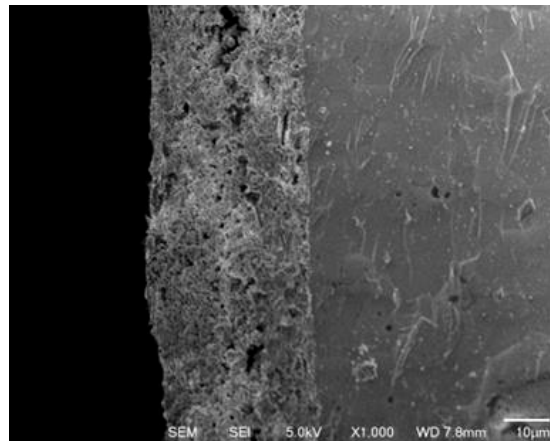
Figure 3. SEM micrograph of the LSCM/GDCW cathode cross section.

Differently, from the top-view analysis, the LSCM/GDCE and LSCM/GDCW cathodes exhibit quite different morphologies, as shown in Figures 4 and 5.
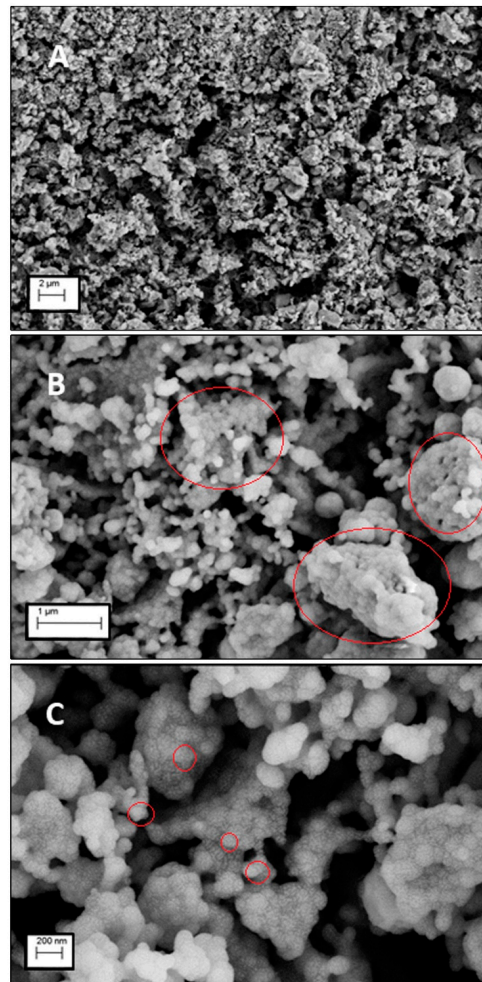

Figure 4. Top view micrographs (fully completed infiltration) of the LSCM/GDCE cathode at increasing magnifications (from (**A**–**C**)). Subfigure (**A**) (lowest magnification) gives evidence of the homogeneity of cathode's porous structure, while the red circles give evidence of the well-dispersed clusters (**B**) of doped-ceria nanoparticles (**C**) alongside the whole electrode's surface.
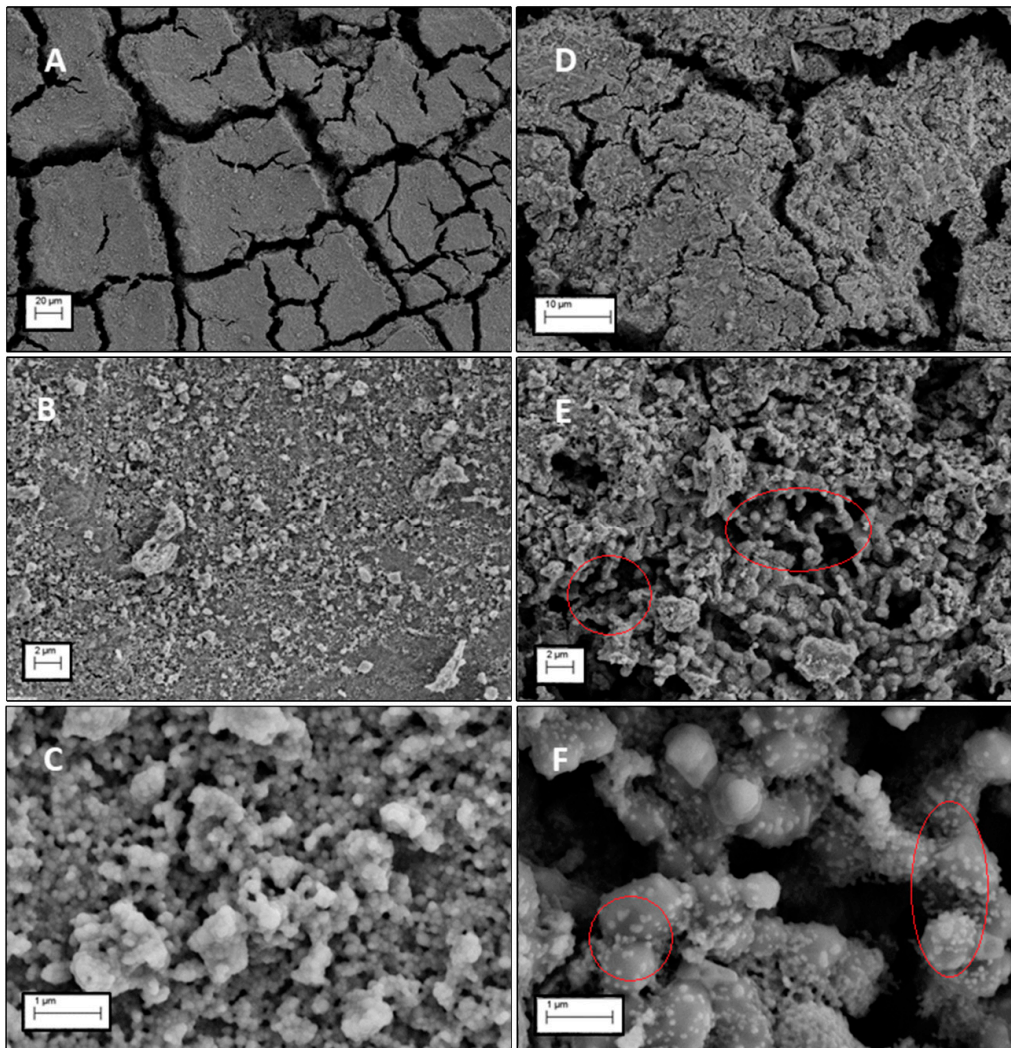
Figure 5. Top-view micrographs (fully completed infiltration) of the LSCM/GDCW cathode at different magnifications: external layer (**A**–**D**) and internal electrode (**E**,**F**). Subfigures from (**A**–**D**) have been taken on the outer surface, while subfigures (**E**,**F**) have been taken inside the crevices clearly visible in (**A**,**D**). Doped-ceria nanoparticles (in red circles) are poorly accessible, as they can only be observed considerably deep inside the electrode.

At low magnification, the LSCM/GDCE surface (Figure 4A) seems porous, with the presence of micrometric clusters (Figure 4B) covered by GDC nanometric grains of about 100 nm (Figure 4C). The measured size value is very similar to the GDC crystallite size calculated using the Scherrer equation.

Otherwise, the LSCM/GDCW surface shows dense and compact zones separated by micrometric cracks (Figure 5A). At higher magnification, the LSCM/GDCW compact areas look quite dense (Figure 5B), different to the LSCM/GDCE (Figure 4B). Thus, agglomeration phenomena tend to fill up the surface porosity and these features reasonably occur after each calcination step. The tendency to agglomerate is well known for oxides deriving from aqueous solution precipitation [29–31]. To overcome this limitation, the use of some final washing cycles with ethanol can remove the water molecules from the surface of the particles and hinder the formation of an oxo-bridging bond [35].

Thus, when an aqueous solution was used for the infiltration, the GDC did not properly penetrate inside the porous LSCM backbone and only a small amount of the GDC reached the interface with the electrolyte. Figure 5C,D confirms the presence of dispersed and not interconnected GDC nanoparticles in the interior electrode.

Thus, the microstructure observed can be related to the infiltration procedure reported in Figure 1. The constant GDC loading and the reduced number of infiltrations of the GDCE are in agreement with the observed open-surface porosity that induces a continuous GDC pathway in the backbone; differently, the non-linear loading and the larger amount of infiltration of the GDCW can be related to a less porous electrode surface that prevents a proper and homogeneous infiltration. So, in the LSCM/GDCW cathode, the GDC particles stack together on the external surface of the electrode, while in the LSCM/GDCE a much more uniform distribution of Gd-doped ceria inside the electrode occurs.

Therefore, the noticeable morphological differences emerging from the SEM micrographs between infiltrated cathodes may affect the electrochemical behavior. Figure 6 shows the Nyquist plots at OCV of the LSCM/GDCW and LSCM/GDCE cells operating in a $CO/CO_2 = 30/70$ mixture in the 700–800 °C temperature range. As commonly reported, the impedance spectra show depressed semicircles due to the overlapping of different electrochemical phenomena. Table 1 reports the electrochemical data of the LSCM/GDCW and LSCM/GDCE cells: the ohmic resistance (R_{ohm}) being the high frequency intercept with the real axis, and the polarization resistance (R_{pol}) corresponding to the difference between the high and low frequency intercepts.
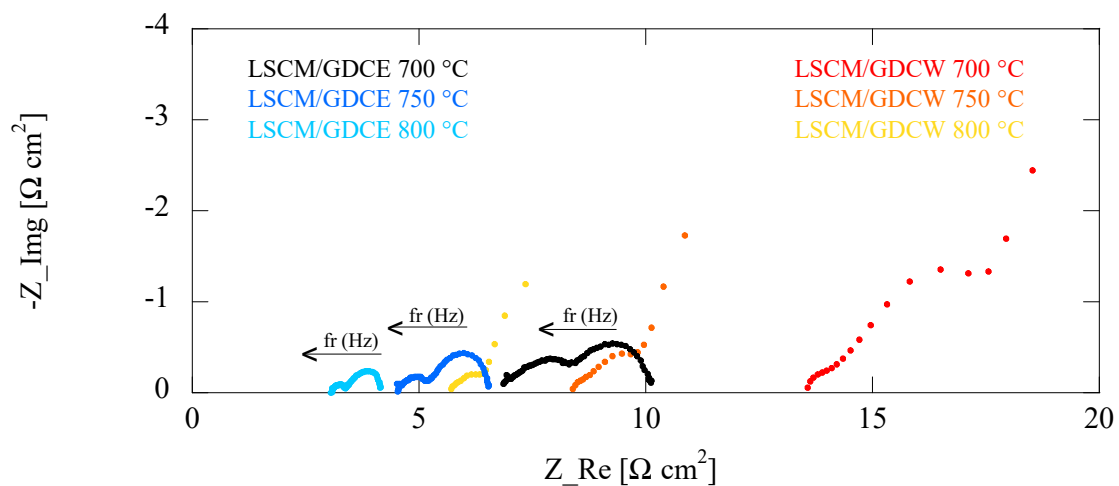

Figure 6. Nyquist plots of the LSCM/GDCW and LSCM/GDCE cells working with CO/CO_2 at different temperatures.

Table 1. R_{ohm} and R_{pol} values of both cells operating in $CO/CO_2 = 30/70$ mixtures at different temperatures.

	LSCM/GDCE		*LSCM/GDCW*	
	R_{ohm} [$\Omega \cdot cm^2$]	R_{pol} [$\Omega \cdot cm^2$]	R_{ohm} [$\Omega \cdot cm^2$]	R_{pol} [$\Omega \cdot cm^2$]
800 °C	3.4	1.1	5.7	4.1
750 °C	4.9	1.9	8.3	11.4
700 °C	6.6	3.2	13.2	21.5

At all temperatures investigated, the R_{ohm} and R_{pol} values of the LSCM/GDCE are lower than those of the LSCM/GDCW. The ohmic resistance (R_{ohm}) is mainly ascribable to the electrolyte but it can be also due to the ohmic contribution of electrodes, thus it is likely that the larger R_{ohm} values of the LSCM/GDCW cell can be ascribable to the agglomeration of GDC nanoparticles on the cathode surface that enhance the ohmic resistance.

At very low frequencies, the impedance spectra of the two cells are quite different. All EIS measurements show at least two semicircles from which it is possible to get the intercept with the real axis at a low frequency and thus evaluate the R_{pol} values. The LSCM/GDCE cell exhibits impedance

spectra comparable to the best performing literature data for similar cells [19,27], while the LSCM/GDCW shows an incomplete Warburg-like behavior at low frequencies, indicating unrestricted diffusion phenomena. Thus, the CO_2 reduction process mostly occurs at the LSCM/GDCE porous cathode and it is related to the cathode microstructure made of well dispersed and interconnected GDC nanoparticles that increase the TPB sites for CO_2 reduction [19].

In order to compare the LSCM/GDCE performance with the state-of-art, the cell has been specifically tested at 900 °C. Figure 7 shows the Nyquist plot of the LSCM/GDCE cell operating with a $CO/CO_2 = 30/70$ mixture at 900 °C alongside the related fitted plot, obtained via software simulation by using the equivalent circuit reported in the inset.
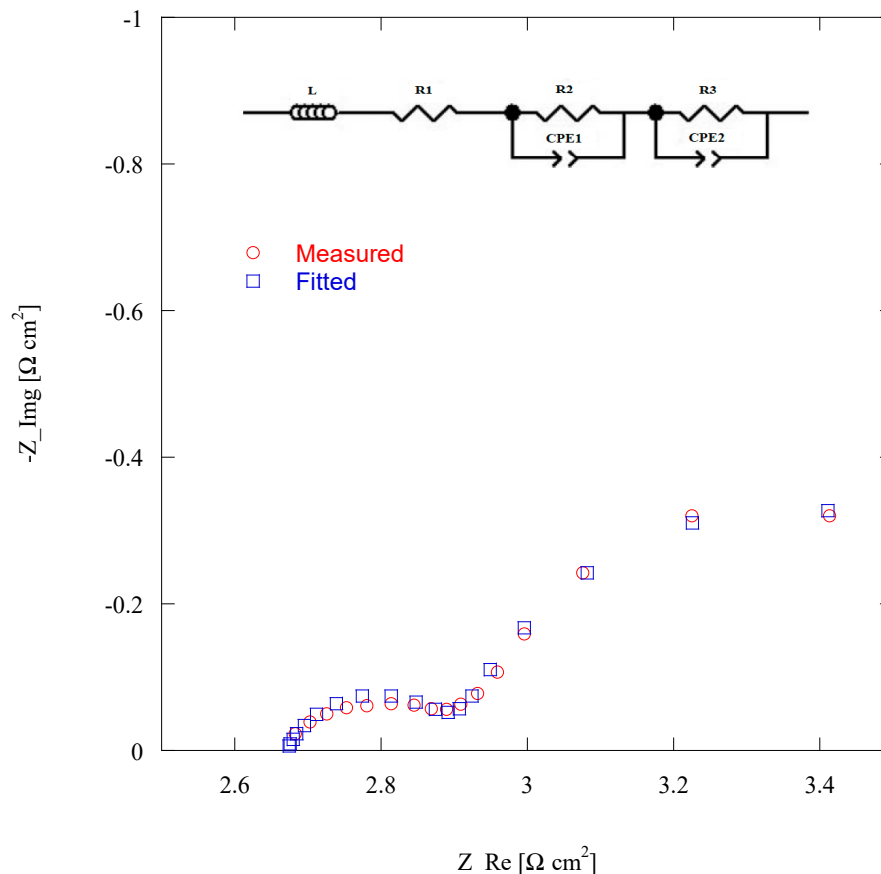

Figure 7. Nyquist plot at OCV of the LSCM/GDCE at 900 °C.

The Nyquist plot was fitted with an $LR_1(CPE_2R_2)(CPE_3R_3)$ equivalent circuit, in which L is the inductance due to the wires of the instrument set up, R_1 is the high-frequency intersection of the plot with the real axis and represents the ohmic resistance (R_{ohm}) of the electrolyte and infiltrated cathode, R_2 is the polarization resistance obtained from the high-frequency (HF) arc and is related to the charge transfer process at the electrode/electrolyte interface, and R_3 is the polarization resistance from the low-frequency (LF) arc and is ascribable to non-charge transfer processes at the electrodes.

The overall polarization resistance ($R_2 + R_3$) value is 0.3 $\Omega \cdot cm^2$, which is comparable to the best performing cathodes from literature. In fact, the conventional Ni-YSZ cathode in the same experimental conditions shows a polarization resistance value of 0.23 $\Omega \cdot cm^2$ and a modified GDC-based cathode with Pd co-catalyst exhibits $R_{pol} = 0.24$ $\Omega \cdot cm^2$ [25].

Finally, Figure 8 shows the Arrhenius plot related to the LSCM/GDCE polarization resistance, exhibiting a good linearity over the whole temperature range investigated (700–900 °C). From the linear fit, an activation energy of the polarization process equal to ~160 kJ mol^{-1} can be derived.

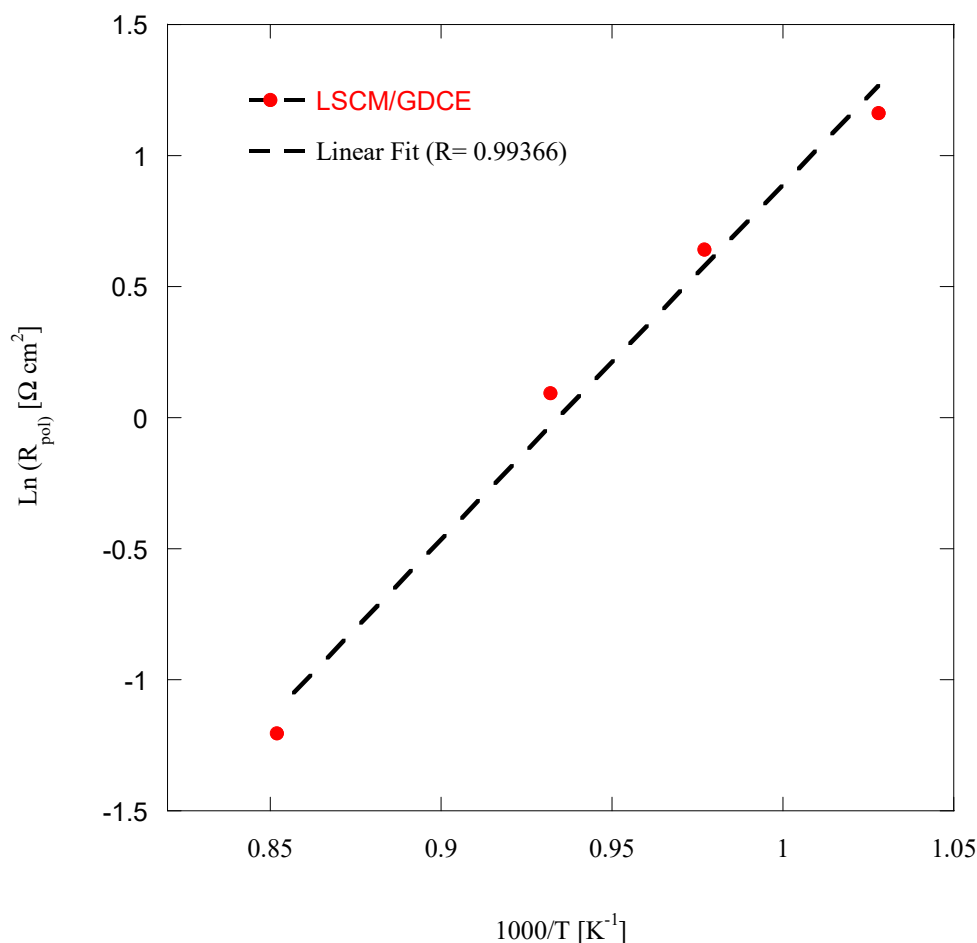**Figure 8.** Arrhenius plot (and related linear fitting) of the LSCM/GDCE working with CO/CO_2.

4. Conclusions

Performing cathodes were fabricated by GDC infiltration into a two-layered LSCM/YSZ backbone. Different infiltrating solutions using water and ethanol as solvents (GDCW and GDCE) were employed, resulting in different microstructures. Specifically, the non-aqueous solution greatly favored the GDC nanoparticles' dispersion by reducing the grain agglomeration and increasing the TPB sites for the process of CO_2 reduction. The GDCE also improved the GDC particles' interconnection, favoring the transfer process at the electrode/electrolyte interface. EIS measurements at OCV performed on both the LSCM/GDCW- and LSCM/GDCE-infiltrated cathodes showed that both the ohmic and polarization resistances of the LSCM/GDCE values were lower than those of the LSCM/GDCW at all temperatures investigated. Moreover, the polarization resistance value of the LSCM/GDCE cathode (0.3 $\Omega \cdot cm^2$ at 900 °C) is comparable to the best performing cathodes. Thus, in agreement with the relevant literature, this work confirms that infiltrated cathodes are promising for SOEC applications. Further improvements can be achieved by optimizing the infiltration parameters of the fabrication procedure.

References

1. Ebbesen, S.D.; Mogensen, M. Electrolysis of carbon dioxide in solid oxide Electrolysis cells. *J. Power Sources* **2009**, *193*, 349–358. [CrossRef]

2. Maiti, D.; Hare, B.J.; Daza, Y.A.; Ramos, A.E.; Kuhn, J.N.; Bhethanabotla, V.R. Earth abundant perovskite oxides for low temperature CO_2 conversion. *Energy Environ. Sci.* **2018**, *11*, 648–659. [CrossRef]

3. Wang, C.C.; Chen, K.; Jiang, T.; Yang, Y.; Song, Y.; Meng, H.; Jiang, S.P.; Lin, B. Sulphur poisoning of solid oxide electrolysis cell anodes. *Electrochim. Acta* **2018**, *269*, 188–195. [CrossRef]

4. Thorson, M.R.; Siil, K.I.; Kenis, P.J.A. Effect of cations on the electrochemical conversion of CO_2 to CO. *J. Electrochem. Soc.* **2013**, *160*, F69–F74. [CrossRef]

5. Cometto, C.; Chen, L.; Lo, P.K.; Guo, Z.; Lau, K.C.; Mallart, E.A.; Fave, C.; Lau, T.C.; Robert, M. Highly selective molecular catalysts for the CO_2-to-CO electrochemical conversion at very low overpotential. contrasting Fe vs Co quaterpyridine complexes upon mechanistic studies. *ACS Catal.* **2018**, *8*, 3411–3417. [CrossRef]

6. Lim, H.K.; Kwon, Y.; Kim, H.S.; Jeon, J.; Kim, Y.H.; Lim, J.A.; Kim, B.S.; Choi, J.; Kim, H. Insight into the microenvironments of the metal–ionic liquid interface during electrochemical CO_2 reduction. *ACS Catal.* **2018**, *8*, 2420–2427. [CrossRef]

7. Hu, B.; Guild, C.; Sui, S.L. Thermal, electrochemical, and photochemical conversion of CO_2 to fuels and value-added products. *J. CO_2 Util.* **2013**, *1*, 18–27. [CrossRef]

8. Gopalan, S.; Mosleh, M.; Hartvigsen, J.J.; McConnell, R.D. Analysis of self-sustaining recuperative solid oxide electrolysis systems. *J. Power Sources* **2008**, *185*, 1328–1333. [CrossRef]

9. Wang, L.; Perez-Fortes, M.; Madi, H.; Diethelm, S.; Van Herle, J.; Marechal, F. Optimal design of solid-oxide electrolyzer based power-to-methane systems: A comprehensive comparison between steam electrolysis and co-electrolysis. *Appl. Energy* **2018**, *211*, 1060–1079. [CrossRef]

10. Zheng, Y.; Wang, J.; Yu, B.; Zhang, W.; Chen, J.; Qiao, J.; Zhang, J. A review of high temperature co-electrolysis of H_2O and CO_2 to produce sustainable fuels using solid oxide electrolysis cells (SOECs): Advanced materials and technology. *Chem. Soc. Rev.* **2017**, *46*, 1427–1463. [CrossRef]

11. Dell'Agli, G.; Spiridigliozzi, L.; Marocco, A.; Accardo, G.; Frattini, D.; Yoon, S.P. Morphological and crystalline evolution of Sm-(20%mol)–doped ceria nanopowders prepared by a combined co-precipitation/hydrothermal synthesis for solid oxide fuel cell applications. *Ceram. Int.* **2017**, *43*, 12799–12808. [CrossRef]

12. Spiridigliozzi, L.; Dell'Agli, G.; Marocco, A.; Accardo, G.; Yoon, S.P.; Ham, H.C.; Frattini, D. Engineered co-precipitation chemistry with ammonium carbonate for scalable synthesis and sintering of reference Sm-doped Ceria and novel Gd/Pr co-doped Ceria electrolytes for IT-SOFCs. *J. Ind. Eng. Chem.* **2018**, *59*, 17–27. [CrossRef]

13. Cho, G.Y.; Lee, Y.H.; Hong, S.W.; Bae, J.; An, J.; Kim, Y.B.; Cha, S.W. High-performance thin film solid oxide fuel cells with Scandia-stabilized zirconia (ScSZ) thin film electrolyte. *Int. J. Hydrogen Energy* **2015**, *40*, 15704–15708. [CrossRef]

14. Spiridigliozzi, L.; Biesuz, M.; Dell'Agli, G.; Di Bartolomeo, E.; Zurlo, F.; Sglavo, V.M. Microstructural and electrical investigation of flash sintered Gd/Sm-doped ceria. *J. Mater. Sci.* **2017**, *52*, 7479–7488. [CrossRef]

15. Biesuz, M.; Spiridigliozzi, L.; Frasnelli, M.; Dell'Agli, G.; Sglavo, V.M. Rapid densification of Samarium-doped Ceria ceramic with nanometric grain size at 900–1100 °C. *Mater. Lett.* **2017**, *190*, 17–19. [CrossRef]

16. Song, Y.; Zhou, Z.; Zhang, X.; Zhou, Y.; Gong, H.; Lu, H.; Liu, Q.; Wang, G.; Bao, X. Pure CO_2 electrolysis over an Ni/YSZ cathode in a solid oxide electrolysis cell. *J. Mater. Chem. A* **2018**, *6*, 13661–13667. [CrossRef]

17. Zhou, Y.; Zhou, Z.; Song, Y.; Zhang, X.; Guan, F.; Lu, H.; Liu, Q.; Miao, S.; Wang, G.; Bao, X. Enhancing CO_2 electrolysis performance with vanadium-doped perovskite cathode in solid oxide electrolysis cell. *Nano Energy* **2018**, *50*, 43–51. [CrossRef]

18. Wang, T.; Wang, J.; Yu, L.; Ye, Z.; Hu, X.; Marnellos, G.E.; Dong, D. Effect of NiO/YSZ cathode support pore structure on CO_2 electrolysis via solid oxide electrolysis cells. *J. Eur. Ceram. Soc.* **2018**, *38*, 5051–5057. [CrossRef]

19. Yue, X.; Irvine, J.T.S. Alternative cathode material for CO_2 reduction by high temperature solid oxide electrolysis cells. *J. Electrochem. Soc.* **2012**, *159*, F442–F448. [CrossRef]

20. Qi, W.; Gan, Y.; Yin, D.; Li, Z.; Wu, G.; Xie, K.; Wu, Y. Remarkable chemical adsorption of manganese-doped titanate for direct carbon dioxide electrolysis. *J. Mater. Chem. A* **2014**, *2*, 6904–6915. [CrossRef]

21. Xu, S.; Li, S.; Yao, W.; Dong, D.; Xie, K. Direct electrolysis of CO_2 using an oxygen-ion conducting solid oxide electrolyzer based on La0.75Sr0.25Cr0.5Mn0.5O3-electrode. *J. Power Sources* **2013**, *230*, 115–121. [CrossRef]

22. Yang, L.; Xie, K.; Wu, L.; Qin, Q.; Zhang, J.; Zhang, Y.; Xie, T.; Wu, Y. A composite cathode based on scandium doped titanate with enhanced electrocatalytic activity towards direct carbon dioxide electrolysis. *Phys. Chem. Chem. Phys.* **2014**, *16*, 21417–21428. [CrossRef] [PubMed]

23. Yoon, S.-E.; Ahn, J.-Y.; Kim, B.-K.; Park, J.-S. Improvements in co-electrolysis performance and long-term stability of solid oxide electrolysis cells based on ceramic composite cathodes. *Int. J. Hydrogen Energy* **2015**, *40*, 13558–13565. [CrossRef]

24. Wang, Y.; Liu, T.; Fang, S.; Chen, F. Syngas production on a symmetrical solid oxide H_2O/CO_2 co-electrolysis cell with Sr 2 Fe 1.5 Mo 0.5 O 6–Sm 0.2 Ce 0.8 O 1.9 electrodes. *J. Power Sources* **2016**, *305*, 240–248. [CrossRef]

25. Yue, X.; Irvine, J.T.S. Modification of LSCM–GDC cathodes to enhance performance for high temperature CO_2 electrolysis using solid oxide electrolysis cells (SOECs). *J. Mater. Chem. A* **2017**, *5*, 7081–7090. [CrossRef]

26. Hong, J.; Balamurugan, C.; Im, H.N.; Jeon, S.Y.; Yoo, Y.S.; Song, S.J. The electrochemical properties of nanocrystalline Gd0.1Ce0.9O1.95 infiltrated solid oxide co-electrolysis cells. *J. Electrochem. Soc.* **2018**, *165*, F132–F141. [CrossRef]

27. Green, R.D.; Liu, C.C.; Adler, S.B. Carbon dioxide reduction on gadolinia-doped ceria cathodes. *Solid State Ionics* **2008**, *179*, 647–660. [CrossRef]

28. Dell'Agli, G.; Spiridigliozzi, L.; Pansini, M.; Accardo, G.; Yoon, S.P.; Frattini, D. Effect of the carbonate environment on morphology and sintering behavior of variously co-doped (Ca, Sr, Er, Pr) Samarium-doped Ceria in co-precipitation/hydrothermal synthesis. *Ceram. Int.* **2018**, *44*, 17935–17944. [CrossRef]

29. Dell'Agli, G.; Mascolo, G.; Mascolo, M.C.; Pagliuca, C. Weakly-agglomerated nanocrystalline $(ZrO_2)_{0.9}$ $(Yb_2O_3)_{0.1}$ powders hydrothermally synthesized at low temperature. *Solid. State. Sci.* **2006**, *8*, 1046–1050. [CrossRef]

30. Spiridigliozzi, L.; Dell'Agli, G.; Biesuz, M.; Sglavo, V.M.; Pansini, M. Effect of the precipitating agent on the synthesis and sintering behavior of 20 mol Sm-Doped Ceria. *Adv. Mater. Sci. Eng.* **2016**. [CrossRef]

31. Lopez-Robledo, M.J.; Silva-Trevino, J.; Molina, T.; Moreno, R. Colloidal stability of gadolinium-doped ceria powder in aqueous and non-aqueous media. *J. Eur. Ceram. Soc.* **2013**, *33*, 297–303. [CrossRef]

32. Mott, M.; Song, J.H.; Evans, J.R.G. Microengineering of ceramics by direct ink-jet printing. *J. Am. Ceram. Soc.* **1999**, *82*, 1653–1658. [CrossRef]

33. Stoyanova, D.; Nickolov, R.; Khristov, M.; Panov, D.; Mehandjiev, D. Catalytic activity of Fe/AC, obtained by impregnation of activated carbon in aqueous and non-aqueous media, to neutralize NO. *J. Porous Mater.* **2009**, *16*, 1–7. [CrossRef]

34. Holland, T.J.B.; Redfern, S.A.T. UNITCELL: A nonlinear least-squares program for cell-parameter refinement and implementing regression and deletion diagnostics. *J. Appl. Crystallogr.* **1997**, *30*, 84. [CrossRef]

35. Shi, J.L. Characteristics of the pore structures in the compacts of ultrafine zirconia powder. *J. Solid State Chem.* **1991**, *95*, 412–416. [CrossRef]